



Short communication

Manganese monoxide nanoparticles adhered to mesoporous nitrogen-doped carbons for nonaqueous lithium–oxygen batteries



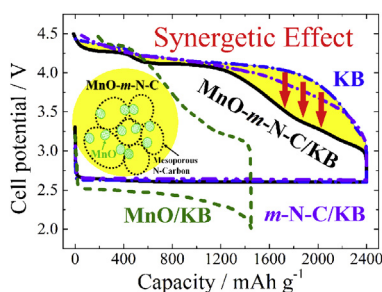
Z.H. Cui, X.X. Guo*

State Key Laboratory of High Performance Ceramics and Superfine Microstructure, Shanghai Institute of Ceramics, Chinese Academy of Sciences, Shanghai 200050, PR China

HIGHLIGHTS

- MnO nanoparticles adhered to mesoporous nitrogen-doped carbons were synthesized.
- Their function in the nonaqueous Li–O₂ batteries was first studied.
- They promote both oxygen reduction and oxygen evolution reactions.
- They especially reduce the charge overpotentials and extend the cycle operation.
- Synergetic effect between the nano-sized MnO and the conductive *m*-N-C plays the role.

GRAPHICAL ABSTRACT



ARTICLE INFO

Article history:

Received 7 January 2014

Received in revised form

12 May 2014

Accepted 13 May 2014

Available online 22 May 2014

Keywords:

Lithium–oxygen batteries

Manganese monoxide nanoparticles

adhered to mesoporous nitrogen-doped carbons

Oxygen reduction and evolution reactions

Synergetic effect

ABSTRACT

Manganese monoxide nanoparticles adhered to mesoporous nitrogen-doped carbons (MnO-*m*-N-C) have been synthesized and their influence on cycle performance of nonaqueous lithium–oxygen (Li–O₂) batteries is investigated. It is found that the MnO-*m*-N-C composites promote both oxygen reduction and oxygen evolution reactions. They lead to reduced charge overpotentials through early decomposition of the Li₂O₂ particles formed on discharge, especially at the limited depth of discharge during the initial several ten cycles. Such superior activity is attributed to the good coupling between the nanosized MnO particles and the conductive mesoporous nitrogen-doped carbons, which is helpful for improving kinetics of both charge and mass transport during the cathode reactions.

© 2014 Elsevier B.V. All rights reserved.

1. Introduction

The rechargeable lithium–oxygen (Li–O₂) battery with a nonaqueous electrolyte has been the focus in recent years, because it may deliver a much larger energy density than state-of-the-art lithium ion battery [1–3]. A typical Li–O₂ battery in most

researches consists of a lithium metal anode, an aprotic lithium conducting electrolyte and an oxygen diffusion cathode with or without a catalyst. In theory, on the cathode the oxygen is reduced to oxygen radical, which reacts with Li⁺ from the electrolyte to form Li₂O₂ upon discharge. Reversibly, the formed Li₂O₂ is decomposed to lithium and oxygen on charge. Nevertheless, for the real application, the cells face more complicated situations due to decompositions of the used electrolytes and carbon-based electrodes, especially when the charge potential over 4.0 V [4–11]. The side products arising from these decompositions cause passivation of

* Corresponding author. Tel.: +86 21 52411032; fax: +86 21 52411802.

E-mail addresses: XXGuo@mail.sic.ac.cn, xiangxin.guo@gmail.com (X.X. Guo).

the air cathode, which further increases the overpotentials in particular for the charge processes, eventually hindering reversible formation and decomposition of the Li_2O_2 [12–14]. Therefore, many efforts have been made in order to promote the oxygen evolution reaction and reduce the charge overpotentials [15–29]. Various kinds of materials such as carbon-based materials [15,16], noble metals [17–21], metal oxides [22,23] and nitrides [24,25], perovskites [26,27], and pyrochlores [28,29] were synthesized and used as catalysts in nonaqueous $\text{Li}-\text{O}_2$ batteries. Among these catalysts, manganese oxides (MnO_x) with various oxide phases as well as different means of preparation have attracted much attention because of their good electrocatalytic activity, low cost and benign character to environment [30,31]. It was reported that the MnO and Mn_2O_3 samples have the similar catalytic activity for oxygen evolution reaction (OER), while the latter being viewed as the best phase of MnO_x for the OER [30]. It was also reported that if composited with conductive carbons the nanosized MnO could have an excellent electrocatalytic activity for oxygen reduction reaction (ORR) [31]. The aforementioned studies of MnO were all carried out in alkaline electrolytes. As a result, it is worthwhile investigating whether such materials have the similar catalytic activities for the $\text{Li}-\text{O}_2$ batteries with the nonaqueous electrolytes, which has not ever been reported according to our knowledge. Moreover, it can be expected that the easily synthesized composites of MnO and conductive carbons can well control the surface morphology and defect chemistry of the cathodes, which are key factors influencing the transport kinetics of electrons, ions and gas species during $\text{Li}-\text{O}$ reactions.

Therefore, in this work, composites of MnO nanoparticles adhered to mesoporous nitrogen-doped carbons ($\text{MnO}-m\text{-N-C}$) are synthesized, and their influence on ORR and OER in the nonaqueous $\text{Li}-\text{O}_2$ batteries is investigated. Note that the selection of nitrogen-doped carbons is not only owing to the fact that they are natural products after synthesis used the method presented here but also because that they presumably can improve the electronic transport property and increase the surface reactivity of carbons [32,33]. It is found that the $\text{MnO}-m\text{-N-C}$ composites have promotion effects on both ORR and OER. Especially for the charge processes, linear sweep voltammetry technique reveals that the $\text{MnO}-m\text{-N-C}$ composites lead to smaller onset potentials of OER than the pure Ketjen-black (KB) carbons. This correlates with early decomposition of Li_2O_2 and the reduced charge overpotentials during cycles in the case of $\text{MnO}-m\text{-N-C}$ incorporated into KB-carbon-based cathodes. The good performance of the composites is attributed to the synergetic effect between the MnO nanoparticles and the conductive $m\text{-N-C}$.

2. Experimental

The synthesis of $\text{MnO}-m\text{-N-C}$ hybrid materials referring to Ref. [31] with some modifications were described in detail in Supplementary Data. TEM and HRTEM measurements were carried out by a JEOL JEM-2100F TEM. XRD analyses of the $\text{MnO}-m\text{-N-C}$ and the discharged/charged electrodes were performed using a Bruker D8-Discover diffractometer. HAADF-STEM and EDS elemental mappings were collected on a FEI Magellan 400 extreme high resolution scanning electron microscope (SEM). Cyclic voltammetry (CV) and linear sweep voltammetry (LSV) were performed in a three-electrode cell with a dual reference electrode [34], a gauze platinum counter electrode in area of 1 cm^2 , and a working electrode consisting of a glass carbon in diameter of 3 mm coated with $\text{MnO}-m\text{-N-C}$ or KB carbons. The loading of $\text{MnO}-m\text{-N-C}$ or KB was 0.1 mg cm^{-2} . Two-electrode $\text{Li}-\text{O}_2$ cells in Swagelok-type were assembled in an Ar-filled glove box (M-Braun, Germany) with both moisture and oxygen content below 0.1 ppm. Components for each

battery include a 0.25-mm-thick lithium anode, a glass fiber ($\Phi 12\text{ mm}$, GF/B, Whatman) separator saturated with 1 M $\text{LiCF}_3\text{SO}_3\text{-TEGDME}$ electrolyte ($\text{H}_2\text{O} < 5\text{ ppm}$), and an air cathode in diameter of 10 mm. The air cathodes were constructed from a slurry consisting of the $\text{MnO}-m\text{-N-C}$, KB carbons and the polyvinylidene difluoride (PVDF) binder in a weight ratio of 45:45:10, or sole KB carbons with the PVDF binder (weight ratio 90:10), which was pasted on a microporous polyethylene (PE) separator (Asahi Kasei Co.) with a thickness of 20 μm and dried in vacuum at 60°C for 12 h. After assembly, each $\text{Li}-\text{O}_2$ battery was sealed in a home-made airtight stainless steel chamber with an inlet and outlet tube for oxygen flowing. With oxygen flowing, the cells were firstly rested for 4 h, and then measured using an Arbin BT2000 cycler. The values of discharge–charge capacities were calculated using the weight of active materials. After measurement, the discharged or charged cathodes were taken out from the cells in the Ar-filled glove box, washed with CH_3CN (purified with fresh activated molecular sieve, $\text{H}_2\text{O} < 4\text{ ppm}$) and dried under vacuum. Then they were used for XRD and SEM characterizations. Note that all those samples were treated carefully without exposing to ambient air. More details on experiments can be found in Supplementary Data.

3. Results and discussion

Fig. 1 (a) and (b) show the transmission electron microscope (TEM) and high-resolution TEM images of the synthesized $\text{MnO}-m\text{-N-C}$. From these figures, it can be seen that the carbons are hollow and its shells in thickness of approximately 5 nm (Fig. 1(b)). These shells connect with each other and form a continuous conducting network. Inside the hollow carbons, crystalline MnO particles in size of approximately 10 nm can be clearly identified (Fig. 1(b)). Moreover, it can be found that the MnO nanoparticles are adhered to the shells of the mesoporous carbons. This feature should be very helpful for transferring electrons from the carbons to the MnO nanoparticles. Fig. 1(c) shows a high-angle annular dark field scanning transmission electron microscopy (HAADF-STEM) image of $\text{MnO}-m\text{-N-C}$ composites. Since the high atomic number Z of elemental Mn, the distribution areas of MnO are imaged as bright spots. Fig. 1(d)–(f) give the energy dispersive spectrometer (EDS) elemental mappings of carbon (1d), oxygen (1e) and manganese (1f). It can be seen that the carbon and oxygen elements are homogeneously distributed in the whole detected area, while the Mn distributed among them separately. The XRD pattern shown in Fig. 1(g) indicated that both the MnO and the carbon shells are crystalline, which are consistent with the HRTEM results shown in Fig. 1(b). Measurement of nitrogen adsorption–desorption isotherms (Fig. 1(h)) reveals a BET surface area of $438\text{ m}^2\text{ g}^{-1}$, and a hysteresis loop in the range of 0.45–1.0 P/P_0 which indicates existence of a mesoporous structure. Calculation of pore size distribution reveals a sharp peak centered at 5 nm (Fig. 1(i)), which is attributed to the mesoscopic pores distributed at the carbon shells. Note that the pore size of the carbons presented here (i.e. 5 nm) is smaller than that of 13 nm in Ref. [31], which is in agreement with the larger specific surface area of $438\text{ m}^2\text{ g}^{-1}$ here in comparison to that of $236\text{ m}^2\text{ g}^{-1}$. In addition, XPS shown in Fig. 1(j) clearly indicates a typical peak of N 1s, which is attributed to nitrogenization of the carbon [35]. This peak can be deconvoluted into three Lorentzian peaks attributed to C–N, C=N and N–O bonds, respectively, as displayed in Figure S1. All the above results demonstrate that the crystalline MnO nanoparticles are embedded in the mesoporous nitrogen-doped carbon shells and the $\text{MnO}-m\text{-N-C}$ composites were successfully prepared.

The first discharge and charge behaviors of the KB-carbon-based cathodes without and with the $\text{MnO}-m\text{-N-C}$ have been investigated in the $\text{Li}-\text{O}_2$ batteries with tetraethylene glycol dimethyl ether

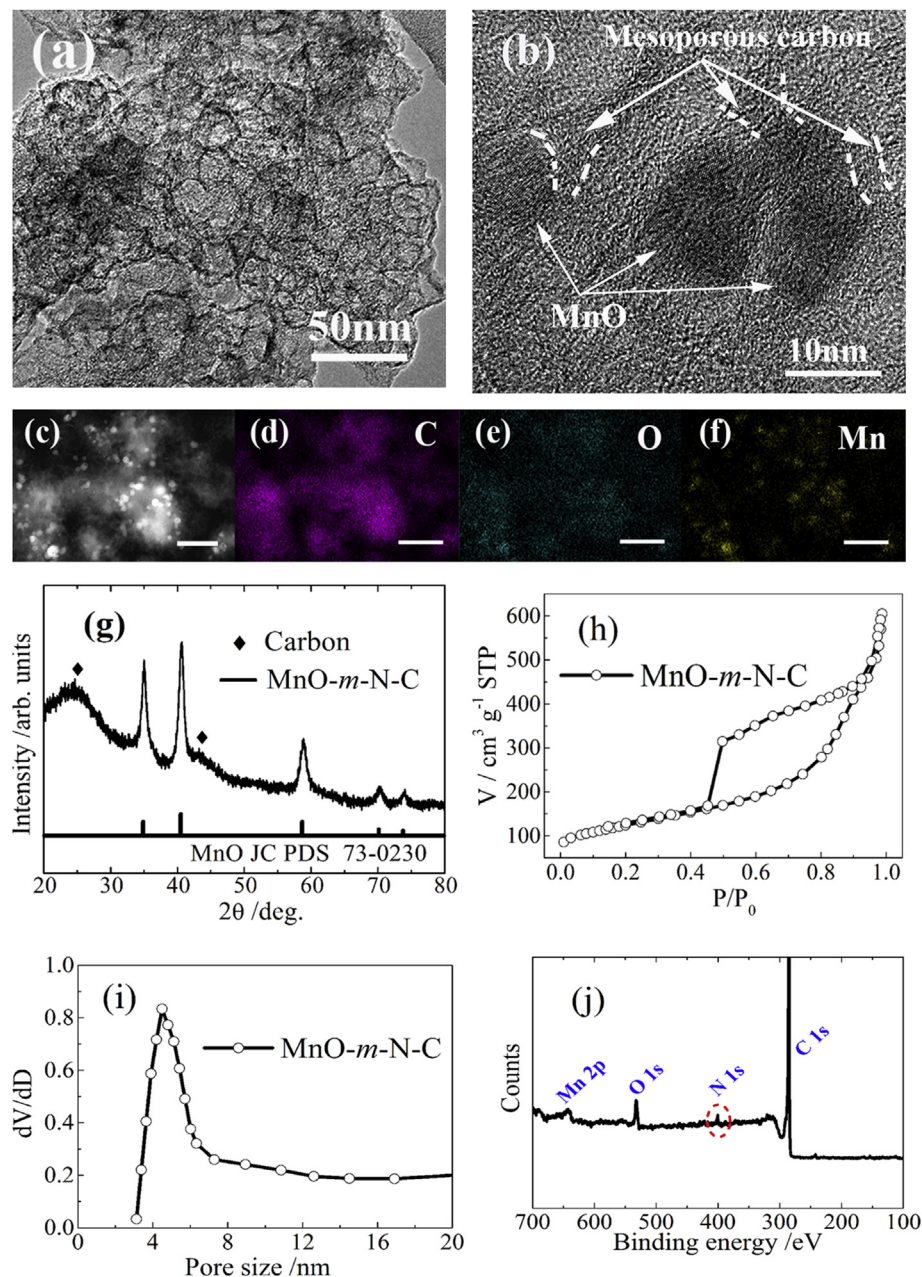


Fig. 1. (a) Representative TEM image and (b) HRTEM image of the MnO-*m*-N-C. (c) HAADF-STEM image of MnO-*m*-N-C and the corresponding EDS elemental mappings of carbon (d), oxygen (e) and manganese (f). The white bars in (c)–(f) represent the scale of 100 nm. (g) XRD pattern of the MnO-*m*-N-C. The pattern of MnO (JCPDS 07-0230) is given for comparison. (h) Nitrogen adsorption and desorption isotherms of the MnO-*m*-N-C and (i) pore size distribution curves. (j) XPS of the MnO-*m*-N-C. The peak from N 1s is marked with the red circle. (For interpretation of the references to color in this figure legend, the reader is referred to the web version of this article).

(TEGDME)-based electrolytes. As shown in Fig. 2 (a), the discharge capacity offered by the cathode composed of both KB and MnO-*m*-N-C is much larger than that resulting from two kinds of composite cathodes prepared by mixing *m*-N-C or MnO (commercial MnO powders ball-milled for 6 h, particle size is about ~500 nm) respectively with KB carbons (*m*-N-C/KB and MnO/KB) and the sole KB carbons. Note that the Li₂O₂ as the dominant products formed upon discharge and decomposed on charge have been confirmed as shown in Figure S2. The above results clearly indicate that more Li₂O₂ are formed owing to the introduction of MnO-*m*-N-C into the cathode. Cyclic voltammetry (CV) scans in the O₂-saturated TEGDME: LiCF₃SO₃ solutions are also carried out for both KB and MnO-*m*-N-C, the results of which are shown in Fig. 2(b). Both

materials exhibit a cathodic peak at approximately 2.5 V and an anodic peak at approximately 3.2 V, corresponding to the oxygen reduction and evolution processes, respectively. It can be seen clearly that the ORR and OER peaks are asymmetrical, which indicates that the two reactions are irreversible. This result is consistent with previous papers [36,37], which demonstrates that the pathways followed on ORR and OER are different. In contrast, the MnO-*m*-N-C shows a higher cathodic current than the KB, further indicating its superior oxygen reduction ability. Note that the surface area of MnO-*m*-N-C (438 m² g^{−1}) is smaller than that of KB (815 m² g^{−1}). The improved ORR should be attributed to the synergistic effect between the MnO nanoparticles and the nitrogen-doped carbons rather than the increase of reactive sites [31,38–40].

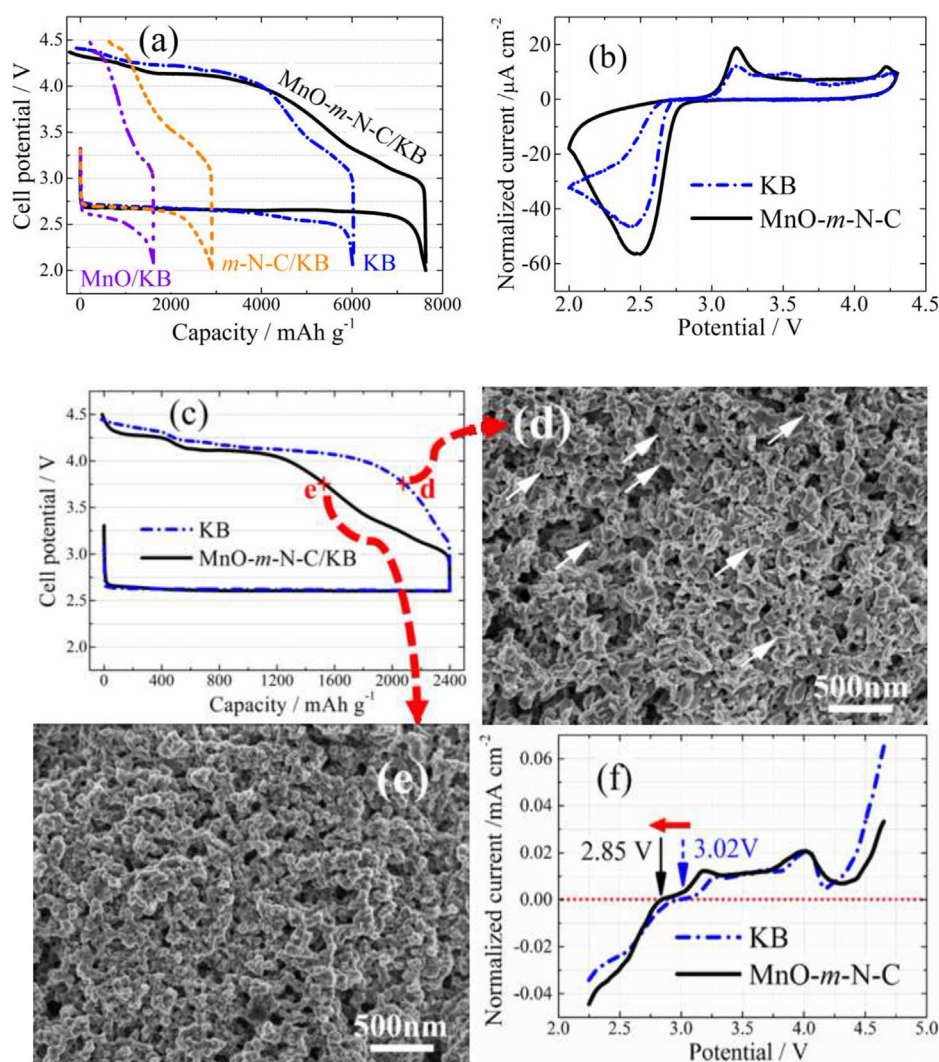


Fig. 2. (a) The first discharge and charge profiles of the KB-based cathodes incorporated with the MnO-*m*-N-C, *m*-N-C and MnO, respectively, and pure KB cathodes, which were tested at a current density of 200 mA g⁻¹ in a voltage range of 2.0–4.5 V. (b) CV curves for the MnO-*m*-N-C and sole KB tested in oxygen saturated 0.1 M LiCF₃SO₃-TEGDME electrolytes with a scan rate of 0.1 mV s⁻¹. The measured potential has been converted to the Li/Li⁺ voltage scale, and the current normalized by the area of glass carbon electrode. (c) The batteries based on the KB carbons without and with the MnO-*m*-N-C, with the *m*-N-C are cycled with the same discharge cutoff capacity of 2400 mAh g⁻¹, except that with MnO discharged to 2.0 V. SEM images for (d) the cathodes composed of the sole KB-carbon cathodes and (e) those with the MnO-*m*-N-C, both of which are recharged to 3.75 V following the discharge to 2400 mAh g⁻¹ (denoted by d and e in the figure). (f) LSV tests of the KB as well as the MnO-*m*-N-C.

In addition, Fig. 2(a) and (b) indicate that the MnO-*m*-N-C leads to the lower charge potential and the larger anodic current in the OER, respectively. To clearly disclose the influence of MnO-*m*-N-C on OER, the batteries based on the KB carbons without and with the MnO-*m*-N-C are discharged with the same capacity cutoff of 2400 mAh g⁻¹, and then recharged to the voltage of ~4.5 V. As shown in Fig. 2(c), the battery with the MnO-*m*-N-C shows lower charge overpotentials compared with that consisting of sole KB carbons, especially in the potential range from 2.9 to 4.0 V. To visualize the effect of MnO-*m*-N-C on promoting decomposition of Li₂O₂, we checked the SEM images for the cathodes composed of sole KB-carbon cathodes and those with the MnO-*m*-N-C, both of which are recharged to 3.75 V following the discharge to 2400 mAh g⁻¹ (Fig. 2(d) and (e)). While many compact small toroid particles (in size of ~200 nm) corresponding to the typical Li₂O₂ crystals are clearly visible on surface of the sole KB cathode (Fig. 2(d)), no such particles can be observed on surface of the KB cathode with the MnO-*m*-N-C composites (Fig. 2(e)). This means that under the same charge condition the MnO-*m*-N-C promotes

the decomposition of Li₂O₂ that is formed during discharge, implying that the MnO-*m*-N-C has a superior promotion influence on OER. In the previous report [22], Nazar et al. found that the Co₃O₄ grown on the reduced graphene oxide (RGO) did not show the conventionally electrocatalytic activity for OER compared to the pure carbon. Instead, it promotes the Li₂O₂ decomposition by enhancing the mass transport. They drew this conclusion because nearly the same onset potentials of OER were detected for the Co₃O₄/RGO on KB and the pure KB-based cathodes by the linear sweep voltammetry (LSV) measurement. To examine whether the MnO-*m*-N-C has the effect similar to or different from the Co₃O₄/RGO, the LSV measurement was carried out on the MnO-*m*-N-C in the TEGDME: LiCF₃SO₃ solution in comparison to that on the KB. Similarly, the glass carbons coated with the testing materials were used as the working electrodes. Each measurement was conducted by firstly holding the voltage at 2.25 V for 1 h to deposit Li₂O₂ on the working electrode, then swept the voltage from 2.25 V to 4.7 V (vs. Li/Li⁺) at a scan rate of 0.1 mV s⁻¹. The current responses monitored during the Li₂O₂ deposition at 2.25 V for the two kinds of electrodes

are shown in Figure S3. Calculation of the equivalent specific capacity corresponding to the above constant-voltage hold indicates that approximately 784 mAh g^{-1} is yielded for the MnO-*m*-N-C and 521 mAh g^{-1} for the KB (detailed calculations are given in the texts following Figure S3). This means that a comparable amount of Li_2O_2 is formed on the two electrodes. As shown in Fig. 2(f), when the potential being scanned from 2.25 V to 4.7 V, while the onset potential of OER for the KB-carbon is approximately 3.0 V, that for the MnO-*m*-N-C is as low as 2.85 V. It is clear that the MnO-*m*-N-C reduces the onset potential of OER by 0.15 V, which is different from the behavior of reported $\text{Co}_3\text{O}_4/\text{RGO}$ [22]. This difference indicates that the MnO-*m*-N-C has a better promotion effect on charge transfer in OER than the previously reported $\text{Co}_3\text{O}_4/\text{RGO}$.

It was recently pointed out that two components of Li-O could be formed during discharge. One is the oxygen-rich $\text{Li}_{2-x}\text{O}_2$ with superoxide-like character formed owing to the porosity of the active carbon, which shows the charge potential ranging from 3.2 V to 3.5 V. The other is the Li_2O_2 , which shows the decomposed potential at approximately 4.2 V [41]. As a result, besides the promotion effect of the MnO-*m*-N-C on OER, its beneficial influence on formation of more oxygen-rich $\text{Li}_{2-x}\text{O}_2$ during discharge could not be excluded for explanation of the reduced charge overpotentials.

In fact, it is worth noting that neither the *m*-C-N nor the pure MnO composites can lead to the same reduced charge potentials as the MnO-*m*-N-C composites (as shown in Fig. 2(a) and (c)). Moreover, the onset potential of OER induced by the MnO is 2.93 V and that by the *m*-C-N is 2.98 V, as revealed by the LSV measurement (Figure S4). Previous reports also indicated that the nitrogen-doped carbons showed no OER activity in the nonaqueous Li-O_2 batteries [42]. As a result, the promoted OER observed here should be attributed to the synergetic effect of the *m*-C-N and the MnO nanoparticles. The good electronic conduction of nitrogen-doped

carbons, reduced size of MnO particles, and their good connection should account for such superior promotion effect. In addition, the full discharge and charge behaviors of the cathodes with MnO-*m*-N-C and KB operated under Ar were also examined. The results are shown in Figure S5, which indicates that the cathodes have no electrochemical activities under Ar atmosphere. Therefore, it can be concluded that the composite of MnO-*m*-N-C and KB exhibits a good catalytic effect on the electrochemical performance of the battery under O_2 .

Cycle performance of the batteries with the MnO-*m*-N-C is investigated as the discharge capacity maintains 800 mAh g^{-1} . Fig. 3 (a) and (b) show the first and 19th cycle curves of the batteries using the KB and MnO-*m*-N-C composites, in comparison to those with the sole KB cathodes. Here the weight ratio of MnO-*m*-N-C versus KB is 1:1, since the cathodes with this ratio exhibit better performance than others in terms of charge overpotential and cycle stability (as can be seen in Figure S6). Furthermore, the homogeneous mixture of MnO-*m*-N-C and KB is important for observing the synergetic effect. As a result, the situation of dispersion of MnO-*m*-N-C with KB was examined by SEM, which is given in Figure S7. It can be seen that the two materials are homogeneously mixed. Fig. 3(a) and (b) indicate that the reduction of charge overpotential occurs in the range of 2.9–4.7 V, in contrast to the range of 2.9–4.0 V in the case of discharge capacity cutoff at 2400 mAh g^{-1} (Fig. 2(c)). This indicates that the influence of MnO-*m*-N-C on charge overpotential becomes more predominant with decreasing depth of discharge. If calculated the charge overpotentials (η_{chg}) by subtracting the thermodynamic equilibrium potential of Li_2O_2 formation (2.96 V vs Li/Li^+) from the potential at the middle point of each slope charge curve, the values of η_{chg} as a function of cycle number can be plotted as shown in Fig. 3(c). It can be found that the charge overpotentials for the battery with the MnO-*m*-N-C are

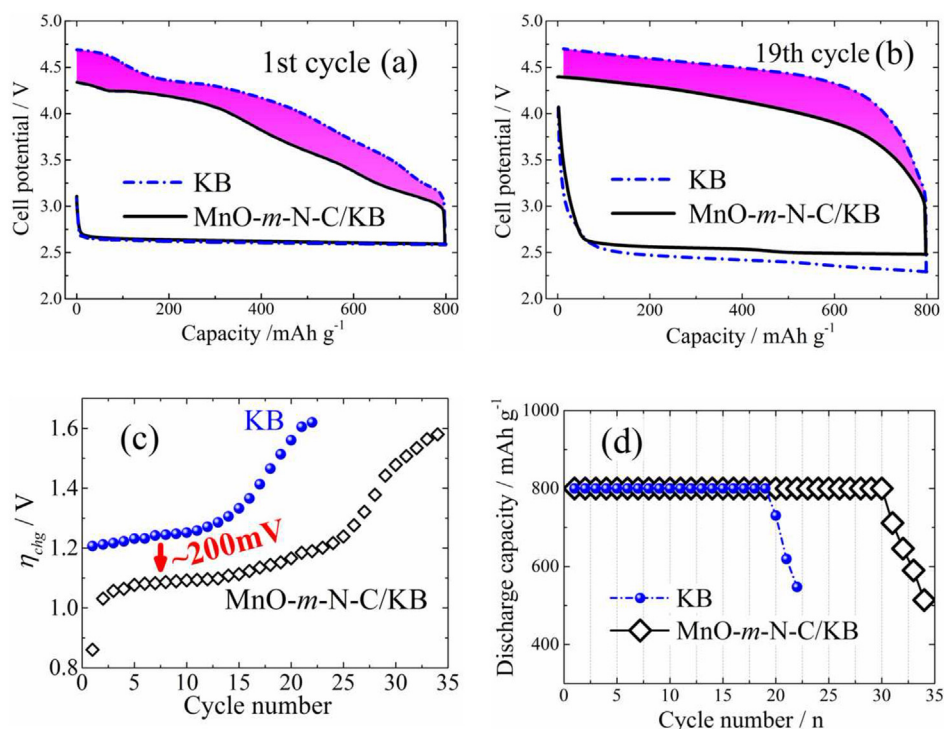


Fig. 3. (a) The first and (b) the 19th cycle curves of the battery with KB-based cathodes with or without the MnO-*m*-N-C composites, which were tested at a current density of 200 mA g^{-1} in a voltage range of 2.0–4.65 V. (c) The charge overpotential (η_{chg}) as a function of cycle number for the KB-based cathodes with or without the MnO-*m*-N-C composites. Each value of η_{chg} is calculated by subtracting the thermodynamic equilibrium potential of Li_2O_2 formation (2.96 V vs Li/Li^+) from the potential at the middle point of the slope charge curve of (a) and (b), respectively. (d) The discharge capacity as a function of cycle number for the KB-based cathodes with or without the MnO-*m*-N-C composites.

approximately 0.2–0.4 V smaller than those for the battery without it. Moreover, as shown in Fig. 3(d), the battery with the addition of MnO-*m*-N-C runs for 30 cycles with maintaining the initial capacity, whereas the battery without it only runs for only 19 cycles. It is well known that the electrolyte used here (e.g. TEGDME:LiCF₃SO₃) has the stability issue against O₂ radical species, especially after charging [43]. Thus, further reduction of the charge overpotentials and extension of the cycle number should be possible if suppressing the side reactions between the electrolyte and the carbon-based electrode [20,44], which is the direction of our future research.

4. Conclusions

The MnO-*m*-N-C composites are synthesized and their function in the nonaqueous Li–O₂ batteries has been investigated. They promote both oxygen reduction and oxygen evolution reactions. LSV measurements reveal that the MnO-*m*-N-C composites lead to early decomposition of Li₂O₂ compared to the pure KB carbons. This is attributed to the nanosized MnO particles and their good connection with the conductive mesoporous nitrogen-doped carbons, which is beneficial to charge as well as mass transfer in OER. Accordingly, the batteries with the incorporated MnO-*m*-N-C show the reduced charge overpotentials and extended cycle life. These results indicate that the cathodes with improved efficiency for the nonaqueous Li–O₂ batteries are achievable on basis of the synergistic effect between the transition-metal oxides and the conductive carbons.

Acknowledgment

This work was supported by the project supported by the National Key Basic Research Program of China 2014CB921004, Key Project of the Chinese Academy of Sciences under Grant No. KGZD-EW-202-2, Sony Corporation and Science Foundation for Youth Scholar of State Key Laboratory of High Performance Ceramics and Superfine Microstructures (SKL201303). Dr. Keisuke Shimizu, Dr. Hiroyuki Morioka, Dr. Hisashi Kajiura and Dr. Yongming Li are acknowledged for helpful discussions.

Appendix A. Supplementary data

Supplementary data related to this article can be found at <http://dx.doi.org/10.1016/j.jpowsour.2014.05.075>.

References

- [1] K.M. Abraham, Z. Jiang, *J. Electrochem. Soc.* 143 (1996) 1–5.
- [2] G. Girishkumar, B. McCloskey, A.C. Luntz, S. Swanson, W. Wilcke, *J. Phys. Chem. Lett.* 1 (2010) 2193–2203.
- [3] P.G. Bruce, S.A. Freunberger, L.J. Hardwick, J.M. Tarascon, *Nat. Mater.* 11 (2012) 19–29.
- [4] B.D. McCloskey, A. Speidel, R. Scheffler, D.C. Miller, V. Viswanathan, J.S. Hummelshøj, J.K. Nørskov, A.C. Luntz, *J. Phys. Chem. Lett.* 3 (2012) 997–1001.
- [5] W. Xu, J.Z. Hu, M.H. Engelhard, S.A. Towne, J.S. Hardy, J. Xiao, J. Feng, M.Y. Hu, J. Zhang, F. Ding, M.E. Gross, J.-G. Zhang, *J. Power Sources* 215 (2012) 240–247.
- [6] M.M. Ottakam Thotiyl, S.A. Freunberger, Z. Peng, P.G. Bruce, *J. Am. Chem. Soc.* 135 (2013) 494–500.
- [7] S.A. Freunberger, Y. Chen, Z. Peng, J.M. Griffin, L.J. Hardwick, F. Barde, P. Novak, P.G. Bruce, *J. Am. Chem. Soc.* 133 (2011) 8040–8047.
- [8] D.M. Itkis, D.A. Semenenko, E.Y. Kataev, A.I. Belova, V.S. Neudachina, A.P. Sirotnina, M. Havecker, D. Teschner, A. Knop-Gericke, P. Dudin, A. Barinov, E.A. Goodilin, Y. Shao-Horn, L.V. Yashina, *Nano Lett.* 13 (2013) 4697–4701.
- [9] C.O. Laoire, S. Mukerjee, E.J. Plichta, M.A. Hendrickson, K.M. Abraham, *J. Electrochem. Soc.* 158 (2011) A302–A308.
- [10] F. Mizuno, S. Nakanishi, A. Shirasawa, K. Takechi, T. Shiga, H. Nishikoori, H. Iba, *Electrochemistry* 79 (2011) 876–881.
- [11] D. Sharon, V. Etacheri, A. Garsuch, M. Afri, A.A. Frimer, D. Aurbach, *J. Phys. Chem. Lett.* 4 (2013) 127–131.
- [12] Z.H. Cui, W.G. Fan, X.X. Guo, *J. Power Sources* 235 (2013) 251–255.
- [13] W.G. Fan, Z.H. Cui, X.X. Guo, *J. Phys. Chem. C* 117 (2013) 2623–2627.
- [14] X.X. Guo, N. Zhao, *Adv. Energy Mater.* 11 (2013) 1413–1416.
- [15] J. Xiao, D. Mei, X. Li, W. Xu, D. Wang, G.L. Graff, W.D. Bennett, Z. Nie, L.V. Saraf, I.A. Aksay, J. Liu, J.G. Zhang, *Nano Lett.* 11 (2011) 5071–5078.
- [16] Z. Guo, D. Zhou, X. Dong, Z. Qiu, Y. Wang, Y. Xia, *Adv. Mater.* 25 (2013) 5668–5672.
- [17] Y.C. Lu, Z.C. Xu, H.A. Gasteiger, S. Chen, K. Hamad-Schifferli, Y. Shao-Horn, *J. Am. Chem. Soc.* 132 (2010) 12170–12171.
- [18] Z. Peng, S.A. Freunberger, Y. Chen, P.G. Bruce, *Science* 337 (2012) 563–566.
- [19] H.-G. Jung, Y.S. Jeong, J.-B. Park, Y.-K. Sun, B. Scrosati, Y.J. Lee, *ACS Nano* 7 (2013) 3532–3539.
- [20] J. Lu, Y. Lei, K.C. Lau, X. Luo, P. Du, J. Wen, R.S. Assary, U. Das, D.J. Miller, J.W. Elam, H.M. Albishri, D.A. E-Hady, Y.-K. Sun, L.A. Curtiss, K. Amine, *Nat. Commun.* (2013), <http://dx.doi.org/10.1038/ncomms3383>.
- [21] E. Yilmaz, C. Yogi, K. Yamanaka, T. Ohta, H.R. Byon, *Nano Lett.* 13 (2013) 4679–4684.
- [22] R. Black, J.H. Lee, B. Adams, C.A. Mims, L.F. Nazar, *Angew. Chem. Int. Ed.* 52 (2013) 392–396.
- [23] Y. Yang, Q. Sun, Y.S. Li, H. Li, Z.-W. Fu, *J. Power Sources* 223 (2013) 312–318.
- [24] F. Li, R. Ohnishi, Y. Yamada, J. Kubota, K. Domen, A. Yamada, H. Zhou, *Chem. Commun.* 49 (2013) 1175–1177.
- [25] K. Zhang, L. Zhang, X. Chen, X. He, X. Wang, S. Dong, L. Gu, Z. Liu, C. Huang, G. Cui, *ACS Appl. Mater. Interfaces* 5 (2013) 3677–3682.
- [26] K.N. Jung, J.I. Lee, W.B. Im, S. Yoon, K.H. Shin, J.W. Lee, *Chem. Commun.* 48 (2012) 9406–9408.
- [27] J.-J. Xu, D. Xu, Z.-L. Wang, H.-G. Wang, L.-L. Zhang, X.-B. Zhang, *Angew. Chem. Int. Ed.* 52 (2013) 3887–3890.
- [28] S.H. Oh, R. Black, E. Pomerantseva, J.H. Lee, L.F. Nazar, *Nat. Chem.* 4 (2012) 1004–1010.
- [29] S.H. Oh, L.F. Nazar, *Adv. Energy Mater.* 2 (2012) 903–910.
- [30] K.L. Pickrahn, S.W. Park, Y. Gorlin, H.-B.-R. Lee, T.F. Jaramillo, S.F. Bent, *Adv. Energy Mater.* 2 (2012) 1269–1277.
- [31] Y. Tan, C. Xu, G. Chen, X. Fang, N. Zheng, Q. Xie, *Adv. Funct. Mater.* 22 (2012) 4584–4591.
- [32] D.-P. Kim, C.L. Lin, T. Mihalisin, P. Heiney, M.M. Labes, *Chem. Mater.* 3 (1991) 686–692.
- [33] K. Gong, F. Du, Z. Xia, M. Durstock, L. Dai, *Science* 323 (2009) 760–764.
- [34] A.W. Bott, *Curr. Sep.* 14 (1995) 64–68.
- [35] L. Zhao, Y.S. Hu, H. Li, Z. Wang, L. Chen, *Adv. Mater.* 23 (2011) 1385–1388.
- [36] Z. Peng, S.A. Freunberger, L.J. Hardwick, Y. Chen, V. Giordani, F. Bardé, Petr Novák, D. Graham, J.-M. Tarascon, P.G. Bruce, *Angew. Chem. Int. Ed.* 50 (2011) 6351–6355.
- [37] C.O. Laoire, S. Mukerjee, K.M. Abraham, E.J. Plichta, M.A. Hendrickson, *J. Phys. Chem. C* 113 (2009) 20127–20134.
- [38] R. Liu, D. Wu, X. Feng, K. Mullen, *Angew. Chem. Int. Ed.* 49 (2010) 2565–2569.
- [39] G. Wu, N.H. Mack, W. Gao, S. Ma, R. Zhong, J. Han, J.K. Baldwin, P. Zelenay, *ACS Nano* 6 (2012) 9764–9776.
- [40] H.W. Park, D.U. Lee, L.F. Nazar, Z. Chen, *J. Electrochem. Soc.* 160 (2013) A344–A350.
- [41] D. Zhai, H.H. Wang, J. Yang, K.C. Lau, K. Li, K. Amine, L.A. Curtiss, *J. Am. Chem. Soc.* 135 (2013) 15364–15372.
- [42] Y. Li, J. Wang, X. Li, J. Liu, D. Geng, J. Yang, R. Li, X. Sun, *Electrochem. Commun.* 13 (2011) 668–672.
- [43] Stefan A. Freunberger, Yuhui Chen, Nicholas E. Drewett, Laurence J. Hardwick, Fanny Bardé, Peter G. Bruce, *Angew. Chem. Int. Ed.* 50 (2011) 8609–8613.
- [44] Z. Jian, P. Liu, F. Li, P. He, X. Guo, M. Chen, H. Zhou, *Angew. Chem. Int. Ed.* 53 (2014) 442–446.